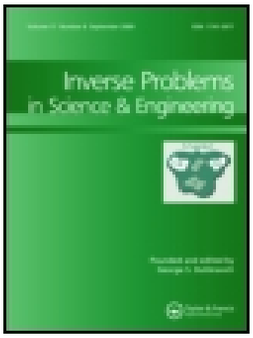

Inverse Problems in Science and Engineering

ISSN: 1741-5977 (Print) 1741-5985 (Online) Journal homepage: http://www.tandfonline.com/loi/gipe20

Numerical reconstruction of brain tumours

Rym Jaroudi, George Baravdish, B. Tomas Johansson & Freddie Åström

To cite this article: Rym Jaroudi, George Baravdish, B. Tomas Johansson & Freddie Åström (2018): Numerical reconstruction of brain tumours, Inverse Problems in Science and Engineering, DOI: 10.1080/17415977.2018.1456537

To link to this article: https://doi.org/10.1080/17415977.2018.1456537

© 2018 The Author(s). Published by Informa UK Limited, trading as Taylor & Francis Group

Published online: 29 Mar 2018.

Submit your article to this journal

Article views: 51

View related articles

View Crossmark data

Full Terms & Conditions of access and use can be found at
http://www.tandfonline.com/action/journalInformation?journalCode=gipe20

INVERSE PROBLEMS IN SCIENCE AND ENGINEERING, 2018
https://doi.org/10.1080/17415977.2018.1456537

Taylor & Francis
Taylor & Francis Group

OPEN ACCESS Check for updates

Numerical reconstruction of brain tumours

Rym Jaroudi[a,b], George Baravdish[a], B. Tomas Johansson[a,c] and Freddie Åström[d]

[a]Department of Science and Technology (ITN), Linköping University, Norrköping, Sweden; [b]LAMSIN-ENIT, Tunis el Manar University, Tunis, Tunisia; [c]EAS Mathematics, Aston University, Birmingham, UK; [d]Heidelberg Collaboratory for Image Processing, Heidelberg University, Heidelberg, Germany

ABSTRACT

We propose a nonlinear Landweber method for the inverse problem of locating the brain tumour source (origin where the tumour formed) based on well-established models of reaction–diffusion type for brain tumour growth. The approach consists of recovering the initial density of the tumour cells starting from a later state, which can be given by a medical image, by running the model backwards. Moreover, full three-dimensional simulations are given of the tumour source localization on two types of data, the three-dimensional Shepp–Logan phantom and an MRI T1-weighted brain scan. These simulations are obtained using standard finite difference discretizations of the space and time derivatives, generating a simple approach that performs well.

ARTICLE HISTORY
Received 13 July 2017
Accepted 13 March 2018

KEYWORDS
Inverse problems; landweber method; nonlinear parabolic equations; reaction–diffusion equations; mathematical biology; medical imaging; three-dimensional simulations of brain tumour growth

AMS SUBJECT CLASSIFICATIONS
65L09; 35K55; 35K57; 65M06; 92B05

1. Introduction

Brain cancer is a common cancer worldwide [1]. In 2012, it was the seventeenth most common cancer. Despite therapeutic progress, brain tumours are still rarely fully curable.

Imaging plays an important role in the diagnosis, follow up and treatment of brain cancer. Medical images provide information about the current state of the tumour, and this information can be used together with mathematical tumour growth models to determine the future state of the tumour given the present (initial) state.

Treatment of brain tumours includes surgery, radiotherapy and chemotherapy and is based on a number of factors, with the location in the brain where the tumour formed being of pivotal importance. Therefore, an effective step to improve brain tumour therapy is to better localize its source. From source localization of brain tumours, clinicians can be provided with new indices that can be used for further diagnosis.

In this work, largely motivated by the potential impact of tumour source localization, we apply techniques from the field of inverse problems to models of reaction–diffusion types, parabolic partial differential equations (PDEs), for locating the source of brain tumours.

CONTACT Rym Jaroudi rym.jaroudi@liu.se

© 2018 The Author(s). Published by Informa UK Limited, trading as Taylor & Francis Group.
This is an Open Access article distributed under the terms of the Creative Commons Attribution-NonCommercial-NoDerivatives License (http://creativecommons.org/licenses/by-nc-nd/4.0/), which permits non-commercial re-use, distribution, and reproduction in any medium, provided the original work is properly cited, and is not altered, transformed, or built upon in any way.

Unlike the majority of the research done in this area, which aim at approximating the nonlinear PDE models by systems of ODEs (for example with the Eikonal equation [2,3]), we propose a novel and altogether different mathematical approach.

We take advantage of the theory of inverse problems to reconstruct the initial data in parabolic equations, that is we recast the source reconstruction as a backward parabolic problem (see Chapter 9 in [4] for an overview of backward problems). In doing this, we work with the reaction–diffusion model directly, and this removes sources of uncertainty introduced when reducing the model to ODEs. Consequently, by bringing in inverse problems into this field, better understanding and quality of the reconstructions can be obtained.

In the work [5], the authors took a basic but well-established model for tumour growth, and presented some mathematical results in terms of existence and uniqueness of a solution in appropriate function spaces. Moreover, the laborious task was undertaken there of doing full three-dimensional numerical simulations of the forward problem to see how the model predicts the tumour growth for various parameters in the model. It is then natural to see how to run the model backwards in time. In [6], an initial study was done for the backward problem in two dimensions. We build on this and extend into three dimensions. Although backward parabolic problems are classical from a theoretical point of view, they still have to be carefully regularized to obtain a stable numerical solution. In the linear case, iterative regularizing methods that preserve the governing partial differential equation have been successfully employed, see the initial works [7–9].

Thus, following these, we propose a nonlinear Landweber method for the regularization. We derive some necessary conditions for convergence, but a full analysis is not the main focus. It is instead presenting three-dimensional numerical simulations showing that stable numerical solutions to the source reconstruction can be obtained. Realistic set up is used in that we use the three-dimensional Shepp-Logan phantom as well as an MRI T1-weighted brain scan as the domain for the numerical experiments. In the simulations, we use different parameters (including nonlinearities) for the forward model compared with the backward model as a way to simulate noise in the data. The analysis and simulations altogether counts as the main novelty of the present work. It is not aimed to get perfectly modelled results; we use a standard widely used model but there are extensions of it for even better prediction of tumour growth. The current work can be seen as an initial start. With the developed techniques one can then make simulations for backward problems for the more advanced tumour models.

For the outline of the work, in Section 2, we present some further background on brain tumours, reaction–diffusion tumour growth models and works related with the brain tumour source localization problem. In Section 3, we propose a Landweber type method applied to the backward reaction–diffusion models for reconstructing the tumour initial state given a later tumour state obtained from a medical image. Then, in Section 4, we describe numerical implementation of the procedure and perform numerical experiments using full three-dimensional imaging data with different source terms, different parameters and different positioning of the tumour. Finally, some conclusions and remarks are given in Section 5.

2. Background on reaction–diffusion models for brain tumour growth

A brain tumour is a mass of abnormally growing normal tissue cells in the brain due to genetic and epigenetic events. Brain tumours are classified according to their origin into primary brain tumours that start in the brain and rarely spreads, and secondary or metastatic brain tumours that have spread to the brain from another location in the body. A growing tumour will eventually compress, shift, invade and damage healthy brain tissue thereby interfering with normal brain functions.

Gliomas are a type of brain tumour that make up about 80% of all malignant brain tumours. According to the World Health Organization (WHO) grading system [10], there are two types of gliomas:

Low-Grade Gliomas (LGG), including grades I and II, are slow growing tumours that look almost normal and infiltrate into normal brain ground tissue. Their progression to a high-grade glioma is almost inevitable [11].

High-Grade Gliomas (HGG), including grade III and IV, look abnormal and are characterized by rapid proliferation, infiltration into large areas. They might also have a necrotic core, form new vascularization to support growth and push the surrounding tissue causing a mass effect [12].

In addition to the uncontrolled proliferation that characterize all types of tumours, brain tumour cells are widely known to be highly diffusive and infiltrating comparing to other types of tumours. Therefore, in order to develop mathematical models describing brain tumour growth, researchers focused on these two main processes namely proliferation and diffusion. As a paradigm, at a given spatial location, new tumour cells appear either by division (proliferation), or by moving from a close location (diffusion).

A well-established model for brain tumour growth was formulated by Murray in [13] as the following reaction–diffusion formalism:

$$\begin{cases} \partial_t u - \operatorname{div}(D\nabla u) - f(u) &= 0, \quad \text{in } \Omega \times (0,T) \\ D\nabla u \cdot n &= 0, \quad \text{on } \partial\Omega \times (0,T) \\ u(x,0) &= \varphi, \quad \text{in } \Omega \end{cases} \tag{1}$$

Here, $u(x,t)$ is the tumour cells density in the spatial position x of the brain region Ω inside the skull at time t. The diffusion term $\operatorname{div}(D\nabla u)$, where div and ∇ are respectively the divergence and the gradient operators, and D the diffusion coefficient, models the 'passive diffusion' (random walk of cells, also called a brownian or fickian process) of tumour cells as a diffusive flux proportional to the gradient of the cell density. It does not model cell migration (that is active motion of cells), nor invasion (that is destruction of the extra-cellular matrix). The reaction term $f(u)$ is the proliferation function of the tumour cells; it describes the growth of the population of tumour cells, which can be exponential $f(u) = \rho u$ with constant proliferation rate ρ, stating that cellular division obeys a cycle, with doubling time $(ln(2)/\rho)$, or logistic $f(u) = \rho u(1-u)$ by decreasing the proliferation parameter ρ in areas of high cellular density. The initial tumour cell density φ is given at time $t = 0$, and the Neumann boundary condition on $\partial\Omega$ states that tumour cells do not diffuse outside the brain region, with the outward unit normal to the boundary being denoted by n.

In early works, the diffusion tensor was considered homogeneous in all of the brain structure Ω: $D = dI$, with I the identity matrix and $d > 0$ a constant value for the diffusion coefficient. Murray et al. in [14] related the velocity v of the moving boundary of the

tumour to the proliferation rate ρ and the diffusion coefficient d such that $v = 2\sqrt{\rho d}$. This work lead the way to studies by Tracqui et al. [15] that gave rise to the first approximations of the model parameters d and ρ using CT scans for HGG. An extension of the model to three dimensions has been done by Burgess et al. in [16] for LGG and HGG.

An improvement to the model done by Swanson et al. in [17] consisted in introducing a diffusion parameter higher in white matter than in grey matter: $D = d(x)I$, where I is the identity matrix and the diffusion coefficient is $d(x) = \begin{cases} d_g & \text{in grey brain tissue} \\ d_w & \text{in white brain tissue} \end{cases}$ where $d_w >> d_g > 0$ are the diffusion coefficients in the white and grey matter, respectively. Swanson et al. in [18] extended the model further to three dimensions taking advantage of the information about white and grey matter areas extracted from the BrainWeb anatomical atlas [19,20]. They showed how the model parameters could be estimated using only in vivo post-contrast T1-weighted and T2-weighted MRI data.

Other extensions to the model have been done, for example, including biomechanical properties of the brain for HGG, [21], and taking into account that glioma cells migrate more easily along the direction of white matter tracts by assuming an anisotropic cell diffusion tensor, deduced from the water diffusion tensor for LGG, [22]. These models were constructed from Diffusion Tensor Imaging (DTI) data.

Besides the prediction of brain tumour growth, this model has been recently used for source localization.

In fact, in [23], Hogea et al. used this model to build an Eulerian framework for modelling tumour growth and its subsequent mechanical impact on the surrounding brain tissue known as the mass-effect and introduced an adjoint-based, PDE-constrained optimization problem to estimate the initial tumour seed. For the numerical experiments, they only provided the one-dimensional case without including real images, brain geometry or tissue heterogeneity. Recently, Gholami et al. in [24], extended this work for LGG by solving the optimization problem with a reduced space Hessian method.

Konukoglu et al. in [2] proposed a different tool to estimate the time elapsed between the emergence of the tumour and its detection. Based on the reaction–diffusion formalism, they deduced the anisotropic Eikonal equation: $\frac{\sqrt{\nabla u \cdot (D \nabla u)}}{\sqrt{\rho} u} = 1$, $u(\partial\Omega) = u_0$, describing the extents of the tumour starting from the visible tumour contour in the MR image. With this, one can obtain ODEs to solve for the cell density rather than a PDE. Later on, Rekik et al. in [3] also used this method with the Powell minimization algorithm to estimate the tumour source location for LGG.

Although challenging to solve due to its nonlinear term, we shall base our reconstruction of the tumour source on the model (2) since it is the standard model used.

3. Source localization

3.1. Backward reaction–diffusion models

Theoretical analysis is not the main aim but numerical implementation. However, as a service to the reader, we include some theory and results on the iterative method to show that it is theoretically underpinned. In principle, on an abstract level, it is known results but we work them out for our nonlinear brain tumour model.

The brain region is denoted by Ω and is a bounded sufficiently smooth region in three-dimensional space. We denote by $H^k(\Omega)$, k a positive integer, the set of all functions u

defined in Ω such that its distributional derivatives of order $|s| = \sum_{i=1}^{k} s_i \leq k$ all belong to $L^2(\Omega)$. Furthermore, $H^k(\Omega)$ is a Hilbert space with the norm

$$\|u\|_{H^k(\Omega)} = \left(\sum_{s \leq k} \int_\Omega \left| \frac{\partial^s u}{\partial x^s} \right|^2 \mathrm{d}x \right)^{1/2}$$

The space $L^p(0, T; H^k(\Omega))$, $p > 1$, consists of all functions u such that for almost every $t \in (0, T)$, the element $u(t)$ belongs to $H^k(\Omega)$. Hence, $L^p(0, T; H^k(\Omega))$ is a normed space with the norm

$$\|u\|_{L^p(0,T;H^k(\Omega))} = \left(\int_0^T \|u\|^p_{H^k(\Omega)} \, \mathrm{d}t \right)^{1/p},$$

where $p > 1$ and k is a positive integer.

We recall the problem

$$\begin{cases} \partial_t u - \operatorname{div}(D\nabla u) - f(u) &= 0, \quad \text{in } \Omega \times (0, T) \\ D\nabla u \cdot n &= 0, \quad \text{on } \partial\Omega \times (0, T) \\ u(0) &= \varphi, \quad \text{in } \Omega \end{cases} \tag{2}$$

with existence of a unique weak solution $u \in L^2(0, T; H^1(\Omega))$ having $u'_t \in L^2(0, T; L^2(\Omega))$, outlined in [5]. For ease of notation, we let $u(x, t) = u(t)$.

The inverse problem we study is to find $u(x, 0)$, where u satisfies the first two equations in (2) and the given final time data $u(x, T) = \psi$.

The operator $A : L^2(\Omega) \to L^2(\Omega)$ is defined by

$$A(\varphi) = u(T) \tag{3}$$

with u the unique (weak) solution to (2). The operator A is in general nonlinear since the governing equation in (2) is nonlinear.

The inverse problem under consideration can then be recast as finding a solution φ to

$$A(\varphi) = \psi. \tag{4}$$

There are results of uniqueness for backward parabolic problems, and we tactically assume that data are such that there exists a unique solution.

To devise a regularizing method for solving the above operator equation, it is important to find what is known as the Fréchet derivative of A. The general definition of this derivative is given in, for example, [25, Chapter 4.2].

For the operator A defined in (3) to have a Fréchet derivative at φ there should exist a linear mapping, denoted $A'(\varphi)$, with

$$A(\varphi + z) - A(\varphi) = A'(\varphi)z + o(\|z\|_{L^2(\Omega)}) \tag{5}$$

for z in a neighbourhood of zero. Here, $o(\|z\|_{L^2(\Omega)})$ means that

$$o(\|z\|_{L^2(\Omega)})/\|z\|_{L^2(\Omega)} \to 0 \quad \text{as} \quad \|z\|_{L^2(\Omega)} \to 0.$$

We shall then verify that A indeed has a Fréchet derivative and give an explicit expression for it. For this, we need the following problem

$$\begin{cases} \partial_t v - \operatorname{div}(D\nabla v) - f_u'(u(\varphi))v &= 0, \quad \text{in } \Omega \times (0,T) \\ D\nabla v \cdot n &= 0, \quad \text{on } \partial\Omega \times (0,T) \\ v(0) &= z, \quad \text{in } \Omega \end{cases} \tag{6}$$

Well posedness of this linear parabolic problem is standard.

We temporarily use the notation $u(\varphi)$ to mean the weak solution to (2) for a given initial element φ, and similarly $v(z)$ is the solution to (6) for a given z. Let

$$w = u(\varphi + z) - u(\varphi) - v(z). \tag{7}$$

One can verify that

$$\begin{cases} \partial_t w - \operatorname{div}(D\nabla w) - f_u'(u(\varphi))w &= F(u,z), \quad \text{in } \Omega \times (0,T) \\ D\nabla w \cdot n &= 0, \quad \text{on } \partial\Omega \times (0,T) \\ w(0) &= 0, \quad \text{in } \Omega \end{cases} \tag{8}$$

where

$$F(u,z) = f(u(\varphi + z)) - f(u(\varphi)) - f_u'(u(\varphi))(u(\varphi + z) - u(\varphi)). \tag{9}$$

Applying standard estimates for weak solutions to parabolic equations, together with the assumption that f is differentiable, it follows that

$$\|w(T)\|_{L^2(\Omega)} \leq o(\|u(\varphi + z) - u(\varphi)\|_{L^2(0,T;(L^2\Omega))}). \tag{10}$$

The solution to (2) depend continuously on the initial data, see [26, 12.2, Remark (b)], thus we can further estimate

$$\|w(T)\|_{L^2(\Omega)} \leq o(\|z\|_{L^2(\Omega)}). \tag{11}$$

Using the definition of the operator A from (3) and the element w given by (7), together with the definition of the Fréchet derivative (5), we conclude that A has a Fréchet derivative at φ, $A'(\varphi)$, and

$$A'(\varphi)z = v(\varphi)(T) \tag{12}$$

with v the solution to (6).

The solution operator of (2) is completely continuous (a weakly converging sequence is turned it a strongly convergent sequence under that operator) viewed as a mapping from $L^2(\Omega)$ to $L^2(0,T;L^2(\Omega))$, see [27, Theorem 10.6 and p. 246] (for a more general result involving also dependence with respect to the coefficients in the equation, see [28]). Since the operator A in (3) is a restriction of the solution to (2) to a fixed instance in time, we conclude that also A is completely continuous. This implies, according to [29, Theorem 4.21], that the Fréchet derivative $A'(\varphi)$ is a compact operator. An equation involving a compact linear operator is the prototype of an ill-posed problem, see for exemple [30]. Thus, simply linearising in (4) will not remove the instability.

Instead, to obtain a stable solution to (4), we apply nonlinear Landweber iterations (updating in the direction of steepest descent),

$$\varphi_{k+1} = \varphi_k - A'^*(\varphi_k)(A(\varphi_k) - \psi). \tag{13}$$

To apply this, we need to find an expression for the adjoint of the Fréchet derivative $A'(\varphi)$, denoted $A'^*(\varphi)$. Now, $A'(\varphi)$ is a linear operator, and one can therefore apply the similar techniques as in [31] to obtain:

Theorem 3.1: *For the adjoint of the Fréchet derivative $A'(\varphi)$, given by (12), let v solve*

$$\begin{cases} \partial_t v + \operatorname{div}(D\nabla v) + f_u'(u(\varphi))v &= 0, \quad \text{in } \Omega \times (0,T) \\ D\nabla v \cdot n &= 0, \quad \text{on } \partial\Omega \times (0,T) \\ v(T) &= z, \quad \text{in } \Omega \end{cases} \tag{14}$$

then

$$A'^*(\varphi)z = v(0). \tag{15}$$

Comparing this expression for the adjoint with the Fréchet derivative (12), we conclude that $A'(\varphi)$ is self-adjoint. Since, as remarked above, $A'(\varphi)$ is a compact operator, spectral theory are at our disposal to analyse $A'(\varphi)$ further, although we shall not pursue it here.

For convergence of the nonlinear Landweber method, we assume that

$$\|A(\varphi) - A(\varphi_0) - A'(\varphi_0)(\varphi - \varphi_0)\| \leq \eta \|A(\varphi) - A(\varphi_0)\| \tag{16}$$

with $0 < \eta < 1/2$. This guarantees convergence provided $\|A'\| \leq 1$, see, for example, [32]. In general, one can introduce a parameter γ to guarantee that the norm is less than or equal unity (that is $\gamma\|A'\| \leq 1$). However, in the numerical experiments, working without a parameter (that is $\gamma = 1$ and hence assuming $\|A'\| \leq 1$) worked fine although improvements can most likely be done by elaborating on this parameter.

It might seem puzzling at first why it is not $\|\varphi - \varphi_0\|$ in the right-hand side of (16) since A is Fréchet differentiable. One has to remember though that we have an ill-posed problem, thus the term $\|\varphi - \varphi_0\|$ can be much larger that $\|A(\varphi) - A(\varphi_0)\|$, making the above estimate more restrictive.

As has been commented on in the literature, it is in general hard to verify (16), that is to find a neighbourhood of φ_0 where this estimate holds. In our case, it might be possible to explicitly find such a neighbourhood due to the estimate (10), however, this would involve technicalities like estimating dependence and size of constants in estimates for quasilinear parabolic equations, and it would take us too far off from the purpose of the present work.

We simply assume that the initial guess of the nonlinear Landweber iterations is sufficiently near the solution of the inverse problem such that (16) holds; the estimate (10) guarantees that it is possible to find such an initial guess.

3.2. Numerical scheme

Following the scheme (13), we start by solving

$$\begin{cases} \partial_t u_1 - \operatorname{div}(D(x)\nabla u_1) - f(u_1) &= 0, \quad \text{in } \Omega \times (0,T) \\ \partial_n u_1 &= 0, \quad \text{on } \partial\Omega \times (0,T) \\ u_1(0) &= \varphi_0, \quad \text{in } \Omega \end{cases} \tag{17}$$

Given that u_k, $k \geq 1$, has been constructed, we proceed by solving the linear adjoint problem

$$\begin{cases} \partial_t v_k + \operatorname{div}(D(x)\nabla v_k) + f_u'(u_k)v_k &= 0, & \text{in } \Omega \times (0,T) \\ \partial_n v_k &= 0, & \text{on } \partial\Omega \times (0,T) \\ v_k(T) &= u_k(T) - \psi, & \text{in } \Omega \end{cases} \tag{18}$$

to obtain v_k. Then u_{k+1} is constructed as the solution to

$$\begin{cases} \partial_t u_{k+1} - \operatorname{div}(D(x)\nabla u_{k+1}) - f(u_{k+1}) &= 0, & \text{in } \Omega \times (0,T) \\ \partial_n u_{k+1} &= 0, & \text{on } \partial\Omega \times (0,T) \\ u_{k+1}(0) &= u_k(0) - v_k(0), & \text{in } \Omega \end{cases} \tag{19}$$

We iterate in the last two steps until the desired level of accuracy has been obtained. In case of noise data a stopping rule is needed to terminate the iterations.

It is straightforward to verify that the above procedure corresponds to the nonlinear Landweber method for solving (4).

4. Numerical simulations

We evaluate the proposed solution scheme on two types of data with synthetically generated tumours obtained via the forward model. We point out that we have avoided what is known as the 'inverse crime' since the constructed data is generated with a different approach and parameters values than the reconstructions.

Rather than doing what is standard in the inverse community to have the same governing model for the forward and inverse problem, we take on the following challenge: the source localization is done using an exponential nonlinearity on a density constructed with the logistic function, and vice versa. We do this, since in real practise we cannot exactly know what nonlinearity was used to generate the data. Thus, with our approach, we do not need to simulate additional noisy data, they are in this sense already noisy. Thus, we ask the reader to bear this in mind when studying the results.

4.1. Data

We use two types of three-dimensional ($3d$) imaging data. The first setting is the standard 3d Shepp-Logan phantom [33] describing a simple geometry, and the second setting is an MRI T1-weighted brain scan [34] from the Internet Brain Segmentation Repository (IBSR) [35] describing a complex geometry.

In the synthetic setting of the 3d Shepp-Logan phantom, we manually selected hypothetical white and grey matter regions as shown in Figure 1. Unlike in the 3d Shepp-Logan image, the MRI data image has ground truth segmentation of white and grey matter regions provided by experts, see Figure 2 for illustration of these regions. In these two figures, the regions are shown on three different and orthogonal planes (slices) through the brain.

Figure 1. Image plane visualizations of a synthetic, but prototypical, segmentation of the 3*d* Shepp-Logan phantom. Ω, which is defined by white and gray regions, corresponding to white and gray matter of the brain, defines the feasible region in which the tumour can evolve.

Figure 2. Ground truth segmentation of an MRI T1 volume where Ω is defined by white and gray colors indicates white and gray matter regions. Tumour growth in this volume is a significantly more challenging problem than the synthetic example shown in Figure 1 due to the presence of many thin and spurious structures, in particularly, made up by white matter tissue as seen in the middle and right panels. Ventricles (black regions encompassed by white and gray matter) are not described by Ω and we do not take into account tissue deformation caused by tumour growth nearby these ventricles, but simply model tumour growth in the white and gray regions. Note that source localization for a tumour grown 'around' a ventricle is harder than a tumour grown in a homogeneous medium since the former case will exhibit severe nonlinear 'retraction' behaviour, which is also confirmed by our evaluation.

4.2. Discretization

For numerical implementation of the reaction–diffusion model, we consider our model as an evolution equation of the form:

$$\partial_t u = Au + f(u),$$

where A is a spatially dependent linear differential operator containing derivatives on its diagonal. The following explicit iterative discretization scheme is used in time due to its simplicity:

$$u^{i+1} = u^i + hAu^i + hf(u^i),$$

where $i = 0, 1, \ldots$, is the current iteration, $h > 0$ is the stepsize and the matrix A, also known as the stencil, can be expressed via a sparse representation making memory requirements less demanding.

We then need to approximate also the spatial derivatives present in A. We adopt a generic forward Euler discretization strategy using finite differences to approximate derivatives in parabolic PDEs [36]. Expanding the divergence term, we have:

$$\operatorname{div}(D\nabla u) = \operatorname{div}\left[\begin{pmatrix} d_{11} & 0 & 0 \\ 0 & d_{22} & 0 \\ 0 & 0 & d_{33} \end{pmatrix}\begin{pmatrix} \partial_x u \\ \partial_y u \\ \partial_z u \end{pmatrix}\right] = \partial_x(d_{11}\partial_x u) + \partial_y(d_{22}\partial_y u) + \partial_z(d_{33}\partial_z u), \tag{20}$$

where the sub-index of d is the corresponding components in terms of rows and columns of D. We point out that the elements of D are dependent on space.

The terms in (20) involve derivatives up to second order. We approximate these derivatives by averaging the forward, ∂^+, and backward, ∂^-, finite difference operators using the following alternating scheme of forward and backward differences for the x-, y- and z-directions:

$$\begin{aligned} \partial_x(d_{11}\partial_x u) &\approx \frac{1}{2}(\partial_x^+(d_{11}\partial_x^- u) + \partial_x^-(d_{11}\partial_x^+ u)) \\ \partial_y(d_{22}\partial_y u) &\approx \frac{1}{2}(\partial_y^+(d_{22}\partial_y^- u) + \partial_y^-(d_{22}\partial_y^+ u)) \\ \partial_z(d_{11}\partial_z u) &\approx \frac{1}{2}(\partial_z^+(d_{33}\partial_z^- u) + \partial_z^-(d_{33}\partial_z^+ u)). \end{aligned} \tag{21}$$

Letting the size of one voxel be 1 (other sizes can easily be adjusted for) given in the x-, y- and z-directions, we derive the forward ∂^+ and backward ∂^- finite difference operators as second order approximations from a third order Taylor series expansion in the x-, y- and z-directions:

$$\begin{aligned} \partial_x^+ u &= u(x+1,y,z) - u(x,y,z) & \partial_y^+ u &= u(x,y+1,z) - u(x,y,z) \\ \partial_x^- u &= u(x,y,z) - u(x-1,y,z) & \partial_y^- u &= u(x,y,z) - u(x,y-1,z) \end{aligned}$$

$$\begin{aligned} \partial_z^+ u &= u(x,y,z+1) - u(x,y,z) \\ \partial_z^- u &= u(x,y,z) - u(x,y,z-1). \end{aligned}$$

From this, we get the approximations:

$$\begin{aligned} \partial_x(d_{11}\partial_x u) \approx \frac{1}{2}[&(d_{11}(x+1,y,z) + d_{11}(x,y,z))(u(x+1,y,z) - u(x,y,z)) \\ &- (d_{11}(x-1,y,z) + d_{11}(x,y,z))(u(x,y,z) - u(x-1,y,z))] \\ \partial_y(d_{22}\partial_y u) \approx \frac{1}{2}[&(d_{22}(x,y+1,z) + d_{22}(x,y,z))(u(x,y+1,z) - u(x,y,z)) \\ &- (d_{22}(x,y-1,z) + d_{22}(x,y,z))(u(x,y,z) - u(x,y-1,z))] \\ \partial_z(d_{33}\partial_z u) \approx \frac{1}{2}[&(d_{33}(x,y,z+1) + d_{33}(x,y,z))(u(x,y,z+1) - u(x,y,z)) \\ &- (d_{33}(x,y,z-1) + d_{33}(x,y,z))(u(x,y,z) - u(x,y,z-1))]. \end{aligned} \tag{22}$$

Since the boundary of Ω is the (curved) boundary of the brain (union of white and grey matter segments), special care is needed when computing the Neumann boundary condition on irregular grids. We approach this problem by sequentially replicating the boundary voxels in the outward normal direction of Ω. Any inconsistency for diagonal flow vectors have not been observed in the simulations, in fact this straightforward strategy performs remarkably well.

Table 1. Description of different experiments.

Parameters						
Construction	$f = \rho u$		$f = \rho u(1-u)$		$f = \rho u$	$f = \rho u(1-u)$
ρ	0.01	0.001	0.01	0.001	0.001	0.01
h	0.05	0.1	0.05	0.1	0.07	0.05
Reconstruction	$f = \rho u$		$f = \rho u(1-u)$		$f = \rho u(1-u)$	$f = \rho u$
ρ	0.001	0.01	0.001	0.01	0.01	0.001
h	0.1	0.05	0.1	0.05	0.02	0.1
Figuers						
3d Shepp-Logan	Figure 3 Figure 5		Figure 11		Figure 15	
T1 MRI	Figure 7 Figure 9		Figure 13		Figure 16	

4.3. Parameters and set-up

For each of the data, we run the model to obtain a synthetic tumour at a time $T > 0$ for a particular parameter configuration. In the Shepp-Logan phantom, we used the diffusivity speed $d_w = 1$ in the white matter and $d_g = 0.05$ in the gray matter segment. For the MRI image, we set diffusivity speed $d_w = 1$ in the white matter region and $d_g = 0.1$ in the grey matter region. We have thereby followed the models biological assumption stating that tumour cells diffuse more rapidly in white matter.

To aid the visualization, we created a numerical routine to render the corresponding 3d planes. In those illustrations, it is in general easier to see the position and growth of the tumour. In the experiments, we place the tumour at various positions to illustrate different scenarios.

To test the sensitivity of the presented approach, we choose to vary the time-step in the Euler scheme and the parameter ρ influencing the degree of the nonlinearity of the source terms in the PDE model (1).

We run the forward problem until $T = 500$ for the Shepp-Logan phantom and the MRI image to construct the grown synthetic tumour ψ that should be extracted from image. The overall problem (17), (18) and (19) is iterated 55 times in order to track improvements in the source localization by performing additional iterations of the outer loop.

In the linear model corresponding to $f(u) = \rho u$, we only need equations (17) and (19) in the overall problem, and the initial condition is updated as $u_{k+1}(0) = u_k(0) - \gamma(u_k(T) - \psi)$ for $\gamma = 1$. Convergence rates and stability results can be found in [7,8] for the linear Landweber type method and in [37] for the nonlinear one.

4.4. Results

For each type of imaging data: the 3d Shepp-Logan image with simple geometry and the T1 MRI data with complex geometry, as mentioned above, we consider constructing the synthetic tumour with different models and reconstructing the source with different models as well, as shown in Table 1.

In the first experiment, we have an exponential reaction term for both the construction and the reconstruction procedures but with different parameters. We let the proliferation rate parameter ρ and the update step h be either 0.01 or 0.001. We test this configuration for two different positions, one which is close to the boundary for both the 3d Shepp-Logan

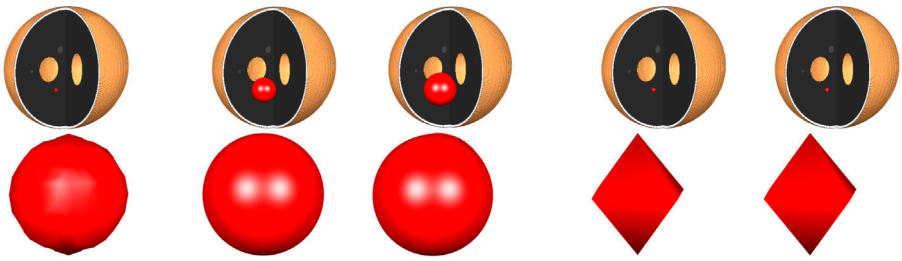

(a) Initial (b) $(\rho, h) = (0.01, 0.05)$ vs $(0.001, 0.1)$ (c) $(\rho, h) = (0.001, 0.1)$ vs $(0.01, 0.05)$

Figure 3. Source localization with exponential reaction terms in construction and reconstruction with large vs. small ρ and small vs. large stepsize h in the 3d Shepp-Logan image.

image and the T1 MRI data. Figures 3–9 illustrate this experiment. To explain the figures containing tumours, such as for example Figure 3, we point out that:

(a) is the initial location and shape to be reconstructed, (b) shows the grown tumours (grown from data in (a)) being the data ψ for two different sets of parameters, and (c) is the corresponding reconstructions of the location with the first figure in (b) used as data for the first reconstruction in (c) and correspondingly the second figure in (b) is used to obtain the second figure in (c) with the parameters as stated. Note that we have stopped the iterations before $t = 0$ by manually tracking and terminated by inspection such that the source is still visible. The single tumours in (c) is the shape of the reconstructed tumour. Note that it is the location that is the main focus. The nonsmooth shape corresponds to the reconstructed tumour occupying only one or a few voxels. There cannot be perfect reconstructions since the data was generated with a different set of parameters. Albeit this, looking at the located position it seems to be a good reconstruction. Error plots as well as errors (see Table 2) verify this.

We have thus varied the parameters ρ and h, and the reconstructions seem stable with respect to these, see further Table 2 for errors with different parameters. To keep down the number of figures, we do not include figures for each set of parameters. We can report that for the 3d Shepp-Logan image, the located tumour source is obtained after 8 iterations when ρ is large and the step size is small and after 10 iterations otherwise for both positions (see Figures 3–6).

However, in the T1 MRI image, it takes 22 and 38 iterations to find the source for large ρ, small step size and small ρ, large step size, respectively (Figures 7–8).

We have varied the position of the source as well. It is more difficult to reconstruct the source when the tumour is near the boundary (ventricles) as shown in Figures 9–10 after 7 iterations.

For the next experiment, we keep the same variations for the parameter ρ and the update step but set the reaction term to be logistic instead. We can report that much the same behaviour as for the exponential term is obtained, see further Table 2. We therefore only include two sets of figures and take then the more difficult case of the tumour near the boundary, see Figures 11–14.

The results obtained for the 3d Shepp-Logan image after 10 and 8 iterations for respectively large and small ρ, small and large step size for the critical position of the tumour are displayed in Figures 11–12. Here, the reconstruction is again difficult when the

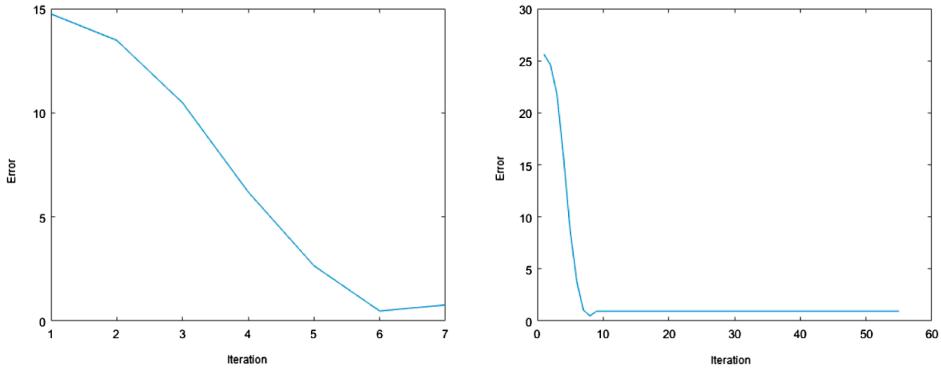

(**a**) small ρ, stepsize 0.1 (**b**) large ρ, stepsize 0.05

Figure 4. Error in source localization with same reaction term $f(u) = \rho u$ in the 3d Shepp-Logan image. The x-axis and the y-axis denote respectively the number of iterations of the nonlinear Landweber method and the relative error in L2 between the exact source and the reconstructed one.

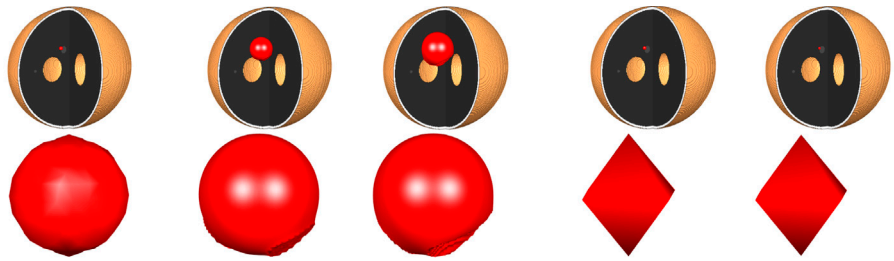

(**a**) Initial (**b**) $(\rho, h) = (0.01, 0.05)$ vs $(0.001, 0.1)$ (**c**) $(\rho, h) = (0.001, 0.1)$ vs $(0.01, 0.05)$

Figure 5. Source localization with exponential reaction terms in construction and reconstruction with large vs. small ρ and small vs. large stepsize h in critical position (on the skull) of the tumour within the 3d Shepp-Logan image.

tumour is near the boundaries (ventricles), ρ is large increasing the nonlinearity and the update step is small. Visually pleasing results are obtained in that the location appear to be accurately identified.

For the MRI data, the results are the same but for different number of iterations: 50 for large ρ and small step while only 4 iterations are needed for the other case, in both cases the tumour is placed near the boundary (Figures 13–14).

Finally, we increase the challenge further by testing mixed reaction terms. For the forward construction, we have a large ρ and step size being 0.05 when f is logistic and a small step size 0.07 when f is exponential. For the reconstruction, it is vice versa except for the step size with the logistic term is set to 0.02.

In the 3d Shepp-Logan setting for Figure 15, all combinations work well with 8 and 9 iterations needed.

Figure 16 shows that the best method here is to consider exponential f for construction and logistic for reconstruction. In fact, despite the complex geometry of the MRI data, the

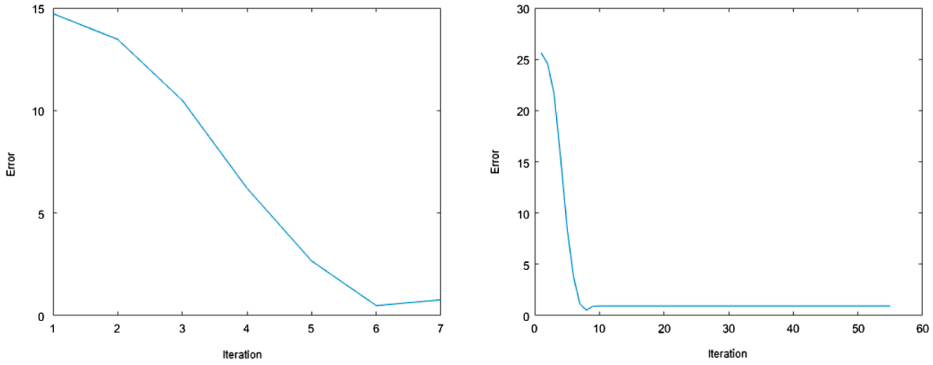

(**a**) small ρ, stepsize 0.1 (**b**) large ρ, stepsize 0.05

Figure 6. Error in source localization with same reaction term $f(u) = \rho u$ in the 3d Shepp-Logan image: the critical tumour position case. The x-axis and the y-axis denote respectively the number of iterations of the nonlinear Landweber method and the relative error in L2 between the exact source and the reconstructed one.

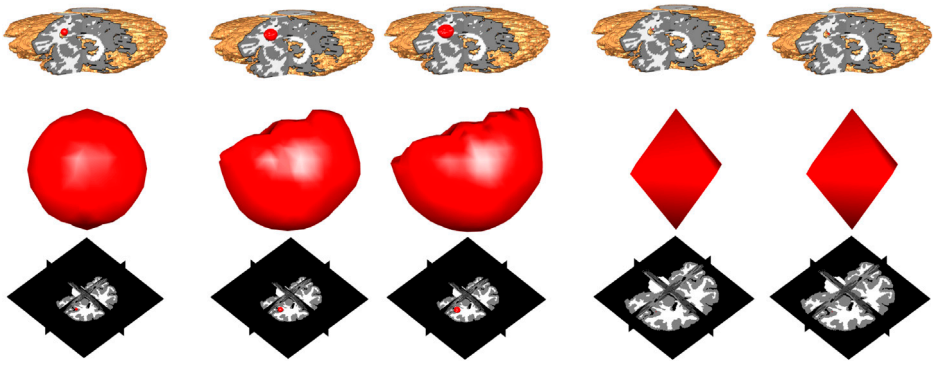

(**a**) Initial (**b**) $(\rho, h) = (0.01, 0.05)$ vs $(0.001, 0.1)$ (**c**) $(\rho, h) = (0.001, 0.1)$ vs $(0.01, 0.05)$

Figure 7. Source localization with exponential reaction terms in construction and reconstruction with large vs. small ρ and small vs. large stepsize h in the T1 MRI image.

source of the tumour was located after only 4 iterations compared to 50 with the other configuration.

To compare between the different methods shown above, we have calculated the relative error in L2 between the ground truth initial density and the estimated tumour source for the 3d Shepp-Logan and the T1 MRI images for the various combinations of reaction terms used (see Tables 2, 3). The results for both imaging data show that the parameter ρ and the update step have important influence on the source reconstruction.

5. Remarks on the numerical simulations

The parameter ρ determines the influence of the source term and a larger value in the construction yields a tumour cell density which is more anisotropic than with smaller

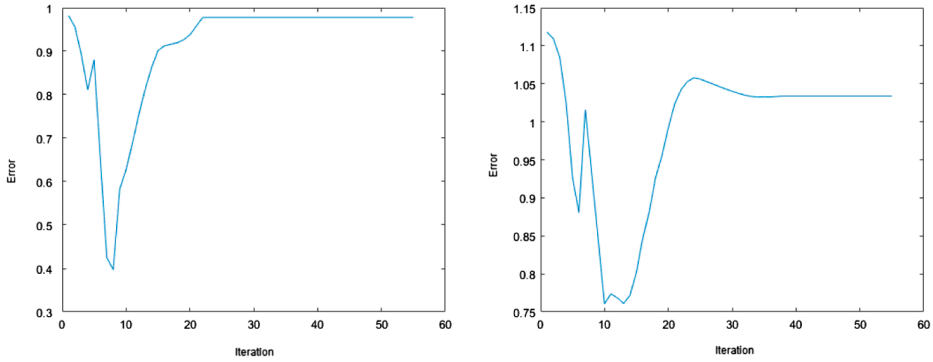

(**a**) small ρ, stepsize 0.1 (**b**) large ρ, stepsize 0.05

Figure 8. Error in source localization with same reaction term $f(u) = \rho u$ in the MRI image. The x-axis and the y-axis denote respectively the number of iterations of the nonlinear Landweber method and the relative error in L2 between the exact source and the reconstructed one.

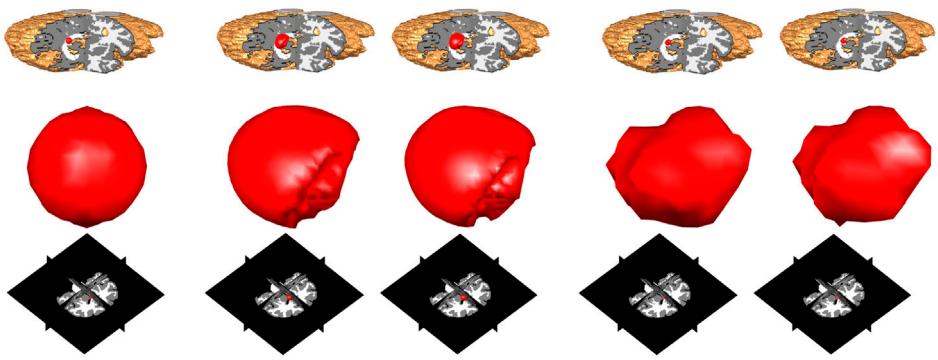

(**a**) Initial (**b**) $(\rho, h) = (0.01, 0.05)$ vs $(0.001, 0.1)$ (**c**) $(\rho, h) = (0.001, 0.1)$ vs $(0.01, 0.05)$

Figure 9. Source localization with exponential reaction terms in construction and reconstruction with large vs. small ρ and small vs. large stepsize h in critical position (on the ventricles) of the tumour within the T1 MRI image.

values, making the source localization in the reconstruction harder. Therefore, it is expected that the error should increase as the value of ρ for the construction increases. This is seen in the figures and errors calculated.

We also remark that when the initial source of the tumour is located close to the boundary it is harder to reconstruct as the proposed regularizing procedure needs to handle a severely anisotropic growth pattern.

The proposed approach assumes that the tumour cell density at the final time (needed as input data) is measurable; typically it would be extracted from medical imagery.

We report that we have also tried the case with the same reaction term but different time-step. This corresponds to the typical noise free case in inverse reconstructions. The above reconstructed location of the source are already good with a rather small relative

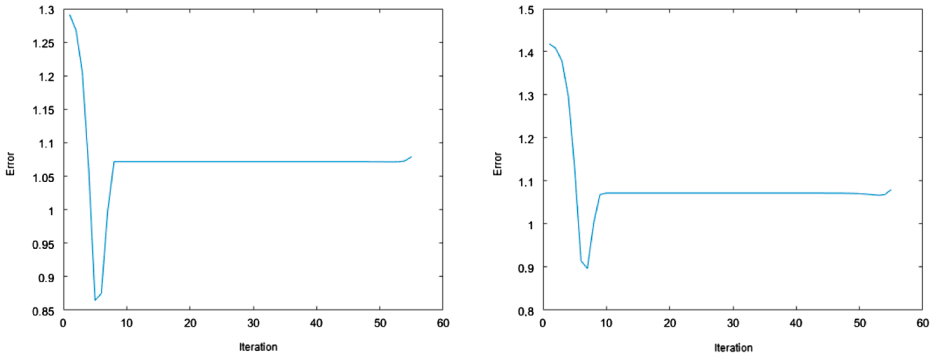

(**a**) small ρ, stepsize 0.1 (**b**) large ρ, stepsize 0.05

Figure 10. Error in source localization with same reaction term $f(u) = \rho u$ in the MRI image corresponding to tumour critical position case. The x-axis and the y-axis denote respectively the number of iterations of the nonlinear Landweber method and the relative error in L2 between the exact source and the reconstructed one.

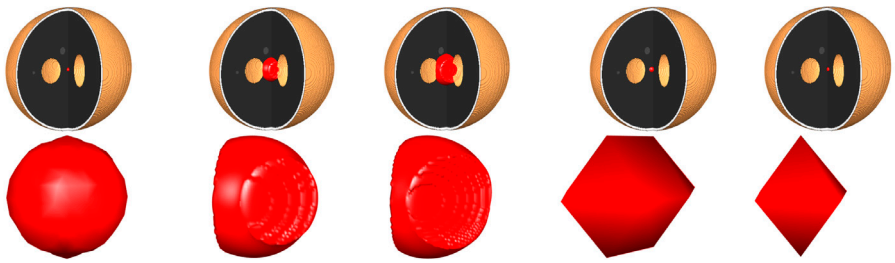

(**a**) Initial (**b**) $(\rho, h) = (0.01, 0.05)$ vs $(0.001, 0.1)$ (**c**) $(\rho, h) = (0.001, 0.1)$ vs $(0.01, 0.05)$

Figure 11. Source localization with logistic reaction terms in construction and reconstruction with large vs. small ρ and small vs. large stepsize h in a critical tumour position (near ventricles) on the 3d Shepp-Logan image.

Table 2. Relative error in L2 between the ground truth initial density and the estimated tumour source for the 3d Shepp-Logan and the T1 MRI images using same reaction terms. Values with $*$ are the critical position of the tumour that is near the ventricles or the skull.

Parameters				
Construction	$f = \rho u$		$f = \rho u(1-u)$	
ρ	0.01	0.001	0.01	0.001
h	0.05	0.1	0.05	0.1
Reconstruction	$f = \rho u$		$f = \rho u(1-u)$	
ρ	0.001	0.01	0.001	0.01
h	0.1	0.05	0.1	0.05
Relative Error in L2				
3d Shepp-Logan	$*$0.76	$*$0.93	$*$0.77	$*$0.79
	$*$0.76	$*$0.93	$*$1.04	$*$1.05
T1 MRI	$*$0.87	$*$0.89	$*$1.05	0.798
	$*$0.79	$*$1.03	$*$1.05	$*$0.93

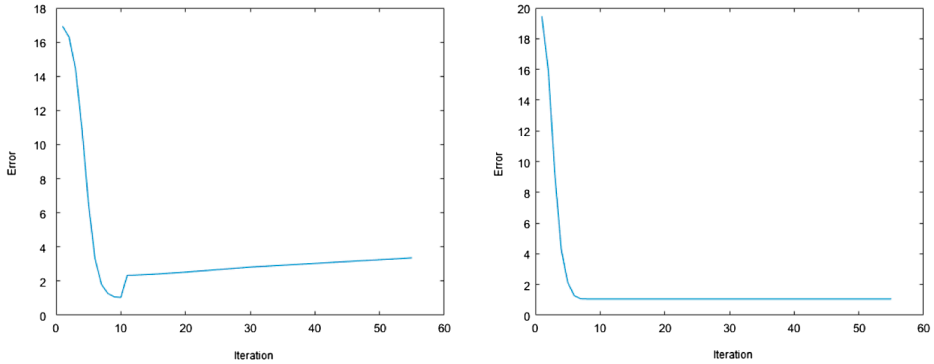

(**a**) small ρ, stepsize 0.1 (**b**) large ρ, stepsize 0.05

Figure 12. Error in source localization with same reactions terms $f(u) = \rho u(1-u)$ in the 3d Shepp-Logan image near the boundary. The x-axis and the y-axis denote respectively the number of iterations of the nonlinear Landweber method and the relative error in L2 between the exact source and the reconstructed one.

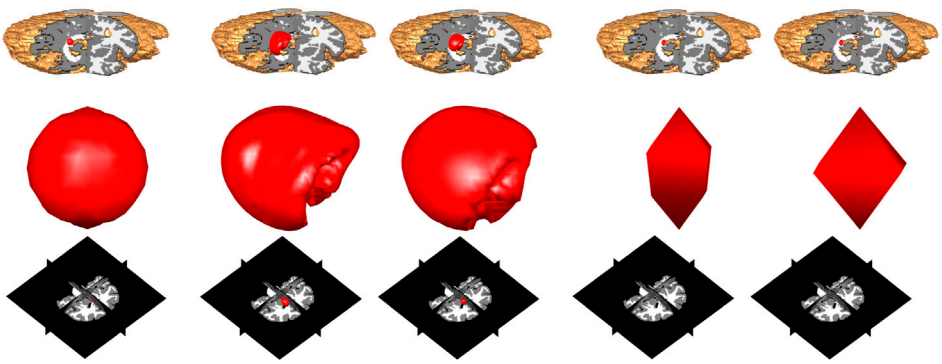

(**a**) Initial (**b**) $(\rho, h) = (0.01, 0.05)$ vs $(0.001, 0.1)$ (**c**) $(\rho, h) = (0.001, 0.1)$ vs $(0.01, 0.05)$

Figure 13. Source localization with logistic reaction terms in construction and reconstruction with large vs. small ρ and small vs. large stepsize h in a critical tumour position (near ventricles) on the T1 MRI image.

Table 3. Relative error in L2 between the ground truth initial density and the estimated tumour source for the 3d Shepp-Logan and the T1 MRI images using different reaction terms.

Parameters		
Construction	$f = \rho u$	$f = \rho u(1-u)$
ρ	0.001	0.01
h	0.07	0.05
Reconstruction	$f = \rho u(1-u)$	$f = \rho u$
ρ	0.01	0.001
h	0.02	0.1
Relative Error in L2		
3d Shepp-Logan	0.93	0.93
T1 MRI	1.00	1.05

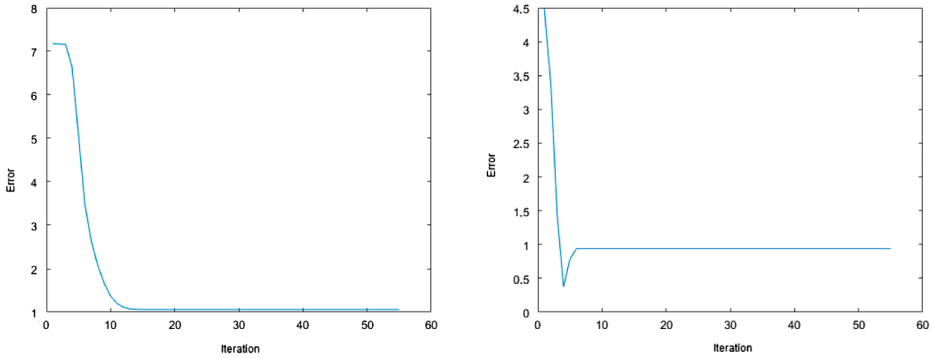

(**a**) small ρ, stepsize 0.1 (**b**) large ρ, stepsize 0.05

Figure 14. Error in source localization with same reaction terms $f(u) = \rho u(1-u)$ in the MRI image. The x-axis and the y-axis denote respectively the number of iterations of the nonlinear Landweber method and the relative error in L2 between the exact source and the reconstructed one.

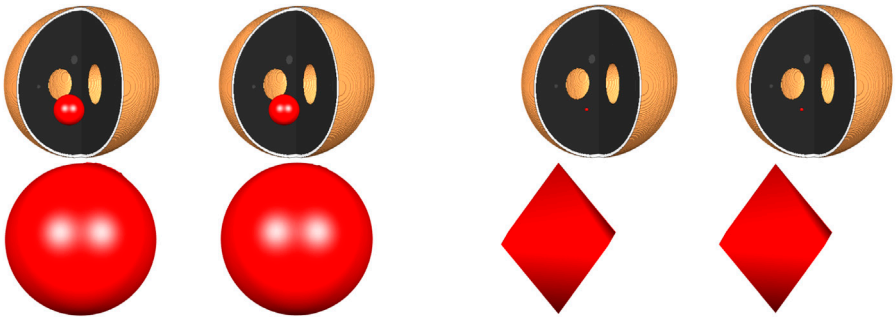

(**b**) $(\rho, h, f) = (0.001, 0.07, exponential)$ vs $(0.01, 0.05, logistic)$ (**c**) $(\rho, h, f) = (0.01, 0.02, logistic)$ vs $(0.001, 0.1, exponential)$

Figure 15. Source localization in the 3d Shepp-Logan image with large vs. small ρ, small vs. large stepsize h and logistic vs. exponential reaction terms in construction and reconstruction respectively.

error. With the same reaction term, this error is decreased further. We choose not to include any figure on this since it is visually not possible to see any comparable difference.

We provide some information about the computations. The numerical simulations presented are done in MATLAB R2016a version 9.0 and executed on an ordinary workstation having an Intel(R) Core(TM) i5-5200U CPU at 2.20 GHz. The total number of voxels in the Shepp-Logan model is $256 \times 256 \times 256$ and for the MRI T1-weighted brain scan it is $256 \times 256 \times 54$ (we do not take into account any differences of resolutions in the x-, y- and z- directions). The total simulation time to generate a set of figures like Figure 3 for the Shepp-Logan model is about 1 hour 40 minutes and to do a set like 9 for the T1 MRI data is around 55 minutes. There is no big difference with respect to the reaction term. No optimization of the code has been done and computational time can therefore be further improved.

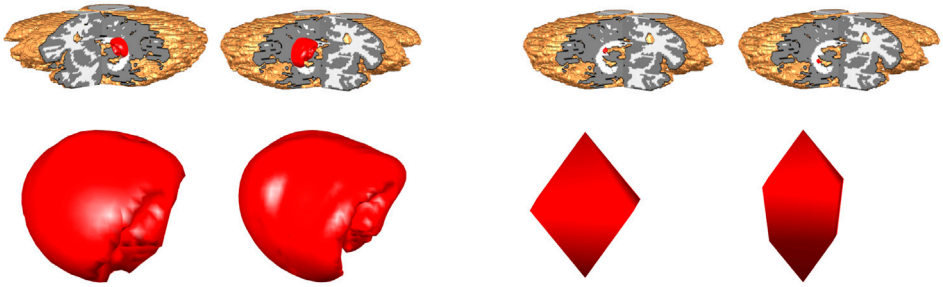

(**b**) $(\rho, h, f) = (0.001, 0.07, exponential)$ vs $(0.01, 0.05, logistic)$

(**c**) $(\rho, h, f) = (0.01, 0.02, logistic)$ vs $(0.001, 0.1, exponential)$

Figure 16. Source localization in the T1 MRI image with large vs. small ρ, small vs. large stepsize h and logistic vs. exponential reaction terms in construction and reconstruction respectively.

6. Conclusion

Reconstruction of tumours backwards in time has been investigated. The problem is formulated as finding the initial state of the solution to a well-established parabolic reaction–diffusion model for tumour growth, given the tumour at a final instance in time. A nonlinear Landweber type method was proposed to obtain a stable solution. Some mathematical analysis was undertaken to find the adjoint operator needed and to motivate convergence. Numerical simulations were performed for two realistic brain models being the three-dimensional Shepp-Logan phantom and an MRI T1-weighted brain scan. An additional challenge was introduced in that the simulations was undertaken with the data generated with a different set of parameters (including different nonlinearities). The obtained results corroborated well with what could be expected theoretically, and indicate that stable numerical results can be obtained opening for further investigations of more advanced tumour growth models backwards in time. Moreover, future perspectives include using extended models covering Diffusion Tensor Imaging type, validation against real data, stability and convergence tests of the numerical schemes.

Disclosure statement

No potential conflict of interest was reported by the authors.

Funding

This work was supported by the EU funding under the program ALYSSA (ERASMUS MUNDUS Action 2, Lot 6).

References

[1] Ferlay J, Soerjomataram I, Dikshit R, et al. Cancer incidence and mortality worldwide: sources, methods and major patterns in globocan. Int J Cancer. 2015;136(5):E359–E386.

[2] Konukoglu E, Clatz O, Menze BH, et al. Image guided personalization of reaction-diffusion type tumor growth models using modified anisotropic eikonal equations. IEEE Trans Med Imag. 2010;29(1):77–95.

[3] Rekik I, Allassonnière S, Clatz O, et al. Tumor growth parameters estimation and source localization from a unique time point: application to low-grade gliomas. Comput Vis Image Underst. 2013;117(3):238–249.
[4] Isakov V. Inverse problems for partial differential equations. New York (NY): Springer-Verlag; 1998.
[5] Jaroudi R, Åström F, Johansson BT, et al. Numerical simulations in 3-dimensions of reaction-diffusion models for brain tumor growth. Manuscript submitted for publication. 2017.
[6] Jaroudi R, Baravdish G, Åström F, et al. Source localization of reaction-diffusion models for brain tumors. In: German Conference on Pattern Recognition; 2016. Cham: Springer; 2016. p. 414–425.
[7] Bastay G. Iterative methods for ill-posed boundary value problems [Dissertations]. Vol. 392, Linkping studies in science and technology. Department of Mathematics, Linkping University, Linkping; 1995.
[8] Kozlov VA, Maz'ya VG. Iterative procedures for solving ill-posed boundary value problems that preserve the differential equations. Algebra Anal. 1989;1(5):144–170.
[9] Hao DN, Lesnic D. The cauchy problem for laplaces equation via the conjugate gradient method. IMA J Appl Math. 2000;65(2):199–217.
[10] Louis DN, Perry A, Reifenberger G, et al. The 2016 world health organization classification of tumors of the central nervous system: a summary. Acta Neuropathol. 2016;131(6):803–820.
[11] Kleihues P, Burger PC, Scheithauer BW. The new who classification of brain tumours. Brain Pathol. 1993;3(3):255–268.
[12] DeAngelis LM. Brain tumors. New Engl J Med. 2001;344(2):114–123.
[13] Murray JD. Mathematical biology II. Spatial models and biomedical applications interdisciplinary applied mathematics. Vol. 18. New York (NY): Springer-Verlag New York Incorporated; 2002.
[14] Murray JD. Mathematical biology I. An introduction interdisciplinary applied mathematics. Vol. 17. New York (NY): Springer-Verlag New York Incorporated; 2001.
[15] Tracqui P. From passive diffusion to active cellular migration in mathematical models of tumour invasion. Acta Biotheoret. 1995;43(4):443–464.
[16] Burgess PK, Kulesa PM, Murray JD, et al. The interaction of growth rates and diffusion coefficients in a three-dimensional mathematical model of gliomas. J Neuropathol Exp Neurol. 1997;56(6):704–713.
[17] Swanson KR, Alvord E, Murray J. A quantitative model for differential motility of gliomas in grey and white matter. Cell Prolif. 2000;33(5):317–329.
[18] Swanson KR, Alvord E, Murray J. Virtual brain tumours (gliomas) enhance the reality of medical imaging and highlight inadequacies of current therapy. Br J Cancer. 2002;86(1):14–18.
[19] Cocosco C, Kollokian V, Kwan R, et al. Brainweb: online interface to a 3d simulated brain database. Neuroimage. 1997;5:S425.
[20] Collins DL, Zijdenbos AP, Kollokian V, et al. Design and construction of a realistic digital brain phantom. In: IEEE Transactions on Medical Imaging. Vol. 3; 1998. p. 463–468.
[21] Clatz O, Sermesant M, Bondiau PY, et al. Realistic simulation of the 3-D growth of brain tumors in MR images coupling diffusion with biomechanical deformation. In: IEEE Transactions on Medical Imaging. Vol. 24; Illinois; 2005. p. 1334–1346.
[22] Jbabdi S, Mandonnet E, Duffau H, et al. Simulation of anisotropic growth of low-grade gliomas using diffusion tensor imaging. Magn Reson Med. 2005;54(3):616–624.
[23] Hogea C, Davatzikos C, Biros G. An image-driven parameter estimation problem for a reaction-diffusion glioma growth model with mass effects. J Math Biol. 2008;56(6):793–825.
[24] Gholami A, Mang A, Biros G. An inverse problem formulation for parameter estimation of a reaction-diffusion model of low grade gliomas. J Math Biol. 2016;72(1–2):409–433.
[25] Zeidler E. Nonlinear functional analysis and its applications. Vol. I. New York (NY): Springer-Verlag; 1986.
[26] Amann H. Nonhomogeneous linear and quasilinear elliptic and parabolic boundary value problems. In: Schmeisser HJ, Triebel H, editors. Function spaces, differential operators and

nonlinear analysis. Vol. 133, Teubner-Texte zur Mathematik. Stuttgart: Teubner; 1993. p. 9–126.
[27] Precup R. Linear and semilinear partial differential equations. Berlin: Walter de Gruyter; 2013.
[28] Coclite GM, Holden H. Stability of solutions of quasilinear parabolic equations. J Math Anal Appl. 2005;308:221–239.
[29] Colton D, Kress R. Inverse acoustic and electromagnetic scattering. 3rd ed. New York (NY): Springer-Verlag; 2013.
[30] Engl HW, Hanke M, Neubauer A. Regularization of inverse problems. Vol. 375. Dordrecht: Springer Science & Business Media; 1996.
[31] Bastay G, Kozlov VA, Turesson BO. Iterative methods for an inverse heat conduction problem. J Inverse Ill-posed Prob. 2001;9:375–388.
[32] Hanke M, Neubauer A, Scherzer O. A convergence analysis of the Landweber iteration for nonlinear ill-posed problems. Numer Math. 1995;72(1):21–37.
[33] Shepp LA, Logan BF. The fourier reconstruction of a head section. IEEE Trans Nucl Sci. 1974;21(3):21–43.
[34] Release name: Male subject. t1-weighted brain scan:788_6. Available from: www.nitrc.org/frs/shownotes.php?release_id=2305.
[35] Ibsr. Internet brain segmentation repository. Available from: www.nitrc.org/projects/ibsr/.
[36] Nocedal J, Wright S. Numerical optimization. In: Springer series in operations research and financial engineering. New York (NY): Springer; 2006.
[37] Schuster T, Kaltenbacher B, Hofmann B, et al. Regularization methods in Banach spaces. Vol. 10. Berlin: Walter de Gruyter; 2012.